ISSN 0021-3640, JETP Letters, 2013, Vol. 98, No. 7, pp. 384–388. © Pleiades Publishing, Inc., 2013.
Original Russian Text © S.I. Ashitkov, P.S. Komarov, M.B. Agranat, G.I. Kanel, V.E. Fortov, 2013, published in Pis'ma v Zhurnal Eksperimental'noi i Teoreticheskoi Fiziki, 2013, Vol. 98, No. 7, pp. 439–444.

Achievement of Ultimate Values of the Bulk and Shear Strengths of Iron Irradiated by Femtosecond Laser Pulses

S. I. Ashitkov, P. S. Komarov, M. B. Agranat, G. I. Kanel, and V. E. Fortov

Joint Institute for High Temperatures, Russian Academy of Sciences, ul. Izhorskaya 13/19, Moscow, 125412 Russia
e-mail: ashitkov11@yandex.ru

Received August 9, 2013

Shock-wave phenomena generated by femtosecond laser pulses in submicron iron film samples have been studied by the interferometric method with the application of frequency-modulated diagnostics in the picosecond time range. The splitting of the shock wave into the elastic and plastic waves with a compression stress of up to 27.5 GPa behind the front of an elastic precursor has been detected. The corresponding maximum shear stress reaches 7.9 GPa, which is even somewhat higher than the calculated ideal shear strength. The measured spall strengths reach 20.3 GPa, which is also comparable to the calculated values of the ideal tensile strength.

DOI: 10.1134/S0021364013200022

The creation of high-power femtosecond lasers made it possible to study the behavior of materials at extremely high rates of the application of mechanical load. This information is necessary for the development of the physical theory of strength and plasticity of materials, construction of models and determining relations for the computational forecasting of intense pulsed actions on materials and constructions in a wide range of the parameters of loading, and creation of the experimental foundation for testing the results of the atomistic simulation of such actions. The results of the first investigations [1–7] of shock-wave phenomena that are generated in thin-film metallic samples by femtosecond laser pulses indicated that shear and tensile stresses close to the extremely possible ("ideal" [8–11]) shear and bulk strengths can be achieved under these conditions. It is also important that experimental data obtained by different methods in a wide range of load durations are described by unified dependences of the resistance to deformation and fracture on the strain rate [12]. These works are of significant interest and stimulate further experimental investigations in this field.

In this work, to continue the previous experimental studies of the dynamics of picosecond shock compression pulses in aluminum, we measure the evolution of shock waves in submicron iron samples. In contrast to aluminum with the fcc structure, iron has the less dense harder bcc crystal structure. Iron undergoes an $\alpha \longrightarrow \epsilon$ polymorphic transition at a pressure of 13 GPa. The high-pressure ϵ phase has the hcp structure. The molecular dynamics calculations [4] indicate the onsets of plastic deformation simultaneously with the $\alpha \longrightarrow \epsilon$ polymorphic transition. The corresponding compression stresses are sensitive to the interparticle interaction potential and vary with change in the shock-compression direction.

The dynamic elastic limit and transition pressure are measured by recording the wave profile of the velocity or pressure. In this work, the interferometric method is used in these measurements for detection with the use of a subnanosecond frequency-modulated (chirped) pulse. Owing to this method, the time dependence of the spatially non-uniform motion of the rear surface of the sample when the shock compression pulse arrives at this surface can be recorded in a single experiment with picosecond time resolution [2, 3, 13–16]. The application of the Fourier analysis of the recorded interference patterns and comparison of the phase distributions obtained before the experiment and in the process of arrival of the compression wave ensure the measurement of the displacement of the target surface with an accuracy of several nanometers. In contrast to multipulse pump–probe methods [1, 16], the single-pulse method ensures much higher reliability of the measurements and can be used to analyze the reproducibility and statistics of shock wave phenomena in thin-film samples.

Pump and probe pulses were generated by a Ti:sapphire laser system that is based on the amplification of chirped pulses and consists of a master oscillator, stretcher, regenerative amplifier, and compressor. A small fraction of a frequency-modulated pulse after the amplifier was guided from the optical unit of the laser and was used to probe shock wave phenomena under study. A frequency-modulated (chirped) probe pulse with a duration of 300 ps, a spectral FWHM of 40 nm, and a central wavelength of 795 nm passed through an optical delay line and arrived at the rear

reflecting surface of the sample, which is a component of a Michelson interferometer.

A higher power pump pulse with a duration of 100 fs behind the compressor was focused on the surface of a plane sample at an angle of 45° by a lens with a focal distance of 30 cm through a glass substrate. The focusing spot had a Gaussian spatial distribution of the intensity with a diameter of 40 μm at a level of $1/e$. The absorption of pump radiation in the surface layer of the metal was accompanied by the generation of a compression pulse, which propagated toward the rear free surface of the sample and moved this surface. The mechanism of the generation of ultrashort shock waves in metals by femtosecond optical pulses was earlier considered in [17]. The energy of pulses was varied by means of a polarization attenuator and was controlled by a calibrated photodetector. After each laser action, the sample under study was displaced to a new place at a distance of about 300 μm by means of a three-coordinate micromanipulator. This ensured the absence of overlapping of modified regions of the target from shot to shot.

We studied 150-μm-thick iron film samples deposited on glass substrates by the magnetron sputtering method. The thickness of the samples measured with an atomic force microscope in the experimental region with an area of about 1 mm^2 was 250 ± 5 and 540 ± 5 nm. Laser irradiation was performed from the side of a glass substrate.

The diagnostic part of the setup was the Michelson interferometer with the imaging configuration, which was connected to an Acton 2300i diffraction spectrometer. A CCD camera at the output of the spectrometer recorded a two-dimensional interference pattern. The longitudinal coordinate of the interference pattern was the sweep of the spectrum of a frequency-modulated probe pulse, where each wavelength corresponded to a certain time instant [15]. The Fourier analysis algorithm applied to two-dimensional interference patterns [18] with the normalization of phase distribution ensured the determination of the phase shift of the probe pulse with an accuracy of $\delta\varphi \approx 0.01$ rad. This accuracy corresponds to the accuracy of the determination of the surface displacement $\delta z \le 1$–2 nm.

The implemented measurement scheme ensured the continuous recording of the displacement of the sample surface as a function of time with the spatial resolution $\delta y \approx 2$ μm in the radial coordinate in the target plane and with the time resolution determined by the dispersion of the spectrometer. The measurement scheme with a diffraction grating with a groove density of 600 grooves/mm ensured the recording of the displacement of the surface in the time interval of 0–230 ps with a time resolution of $\delta t \approx 1$ ps. Calibration of the time interval with the use of the optical delay line showed that the relation between the wavelength and time in the frequency-modulated pulse is linear.

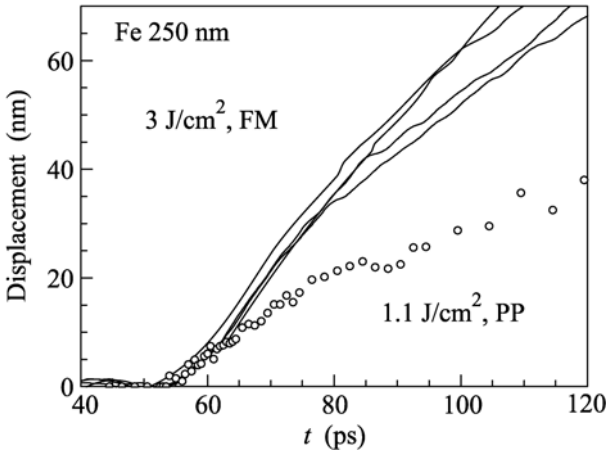

Fig. 1. Displacement histories of the free rear surface of the iron film sample as measured with the use of the (lines, FM) frequency-modulated pulse and (points, PP) pump–probe method at the energy densities of 3 and 1.1 J/cm^2, respectively, in the center of the focal spot. Here and below, zero time is chosen arbitrarily.

As in [19], we observed the limitation of the amplitude of the generated shock compression pulses at the energy densities of pump pulses $F_0 \ge 4$ J/cm^2 because of the optical breakdown in the glass substrate of the target. In view of this circumstance, the experiments were performed at lower energy densities.

Figure 1 shows the experimental results for 250-nm iron film samples at two energy densities in the center of the focal spot of a laser pulse that were obtained with two methods for the recording of the time dependence of the displacement of the sample surface. The profiles were plotted for the central irradiated region with integration over a spatial interval of ±2 μm, which corresponds to the range of variation of the energy density of incident radiation $\Delta F/F_0 = 0.01$. As should be expected, the displacement histories measured in one experiment with the use of the frequency-modulated probe pulse contain a smaller number of chaotic oscillations than that in similar data obtained by the pump–probe method in a series of single-type experiments.

At a constant energy density of a laser pulse, the measurement results in the initial segment of the motion of the surface are well reproducible. A small relative displacement of wave profiles on the time axis in this segment is apparently explained by the variability of the thickness of the sample. The scatter of points in the time dependence of the displacement obtained by the pump–probe method is approximately equal to the relative shift of the displacement histories obtained by the frequency-modulated pulse method. A significant difference in the histories of displacement at times $t \ge 80$ ps is attributed to the spall fracture at the reflection of the compression pulse from the surface, which will be discussed below. The slope of the initial

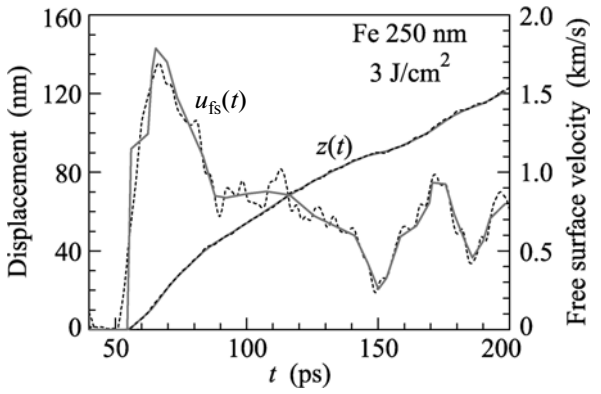

Fig. 2. Example of the processing of one of the displacement profiles $z(t)$ shown in Fig. 1 for the 250-nm-thick sample. The dashed lines are the measured displacement profile and the velocity profile of the free surface obtained by the differentiation of the smoothed profile $z(t)$. The solid lines are obtained by iterative processing.

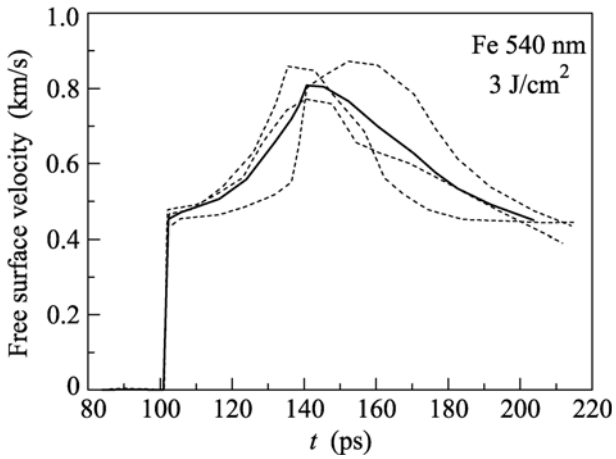

Fig. 3. (Dashed lines) Velocity profiles of the free surface of the 540-nm-thick film sample at an energy density of 3 J/cm^2. The wave fronts are shifted from the average motion beginning time by no more than 1 ps. The solid line is the averaged profile $u_{fs}(t)$.

segment of the displacement profile $z(t)$ and, therefore, the velocity in this segment remain unchanged when the energy density of the laser pulse changes by a factor of 3. At $F_0 = 3$ J/cm^2, a further increase in the velocity follows the initial segment; i.e., two successive compression waves are detected. This feature is absent at $F_0 = 1.1$ J/cm^2.

Figure 2 exemplifies the processing of the displacement history. The velocity history of the free surface was obtained by the differentiation of the experimental dependence $z(t)$ with the subsequent iteration processing that ensures the best correspondence of the integral of the velocity to the measured displacement time dependence.

Figure 3 shows the results of three experiments with 540-nm-thick samples. The amplitude of the first wave is reproduced quite well, whereas the spread of the data increases with time.

Figure 4 shows the averaged velocity profiles of the free surface for 250- and 540-nm-thick film samples. They exhibit strong decay of both the compression pulse as a whole and the first shock wave of the two-wave configuration. The velocity of the first wave front in the range from 250 to 540 nm averaged over all measurements is $U_S = 6.45 \pm 0.2$ km/s. The velocity of the surface behind the first shock wave decreases from 1.06 ± 0.06 km/s at a distance of 250 nm to 0.45 ± 0.03 km/s at a distance of 540 nm.

Comparison of the velocities obtained for the shock wave and particle velocity $u_p = u_{fs}/2$ with the Hugoniot of the ϵ phase of iron [20] shows that the measured velocity of the wave front is much higher than the expected value. Taking into account a short ($\leq$1 ps) rise time of the first wave, the first wave of the detected two-wave configuration is certainly an elastic precursor of the compression wave. Using the average values of the particle velocity behind the precursor front and its propagation velocity, as well as the longitudinal speed of sound at zero pressure $c_l = 5.97$ km/s, we plotted a metastable Hugoniot of iron in the form $U_S = 5.97 \pm 1.2u_p$ km/s. After that, the compression stresses behind the elastic precursor front were calculated by the formula $\sigma_{HEL} = \rho_0 U_S u_{fs}/2$, where ρ_0 is the density of the material, and the values of 27.5 ± 2.5 GPa and 11.0 ± 1 GPa were obtained for the distances of 250 and 540 nm, respectively.

The diagram of states of iron is shown in Fig. 5, where the estimated metastable elastic-compression Hugoniot, the equilibrium adiabat $p(V)$ of the low-pressure α phase, and the Hugoniot with the transition to the high-pressure ϵ phase are plotted. In terms of the deviation of the state behind the precursor front from the equilibrium adiabat of the low-pressure

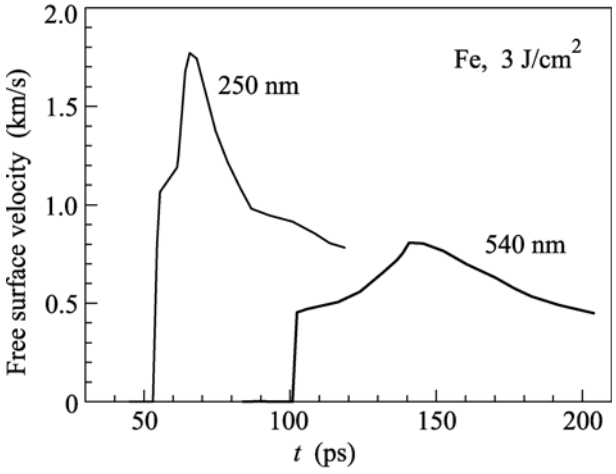

Fig. 4. Evolution of the compression pulses propagating in iron.

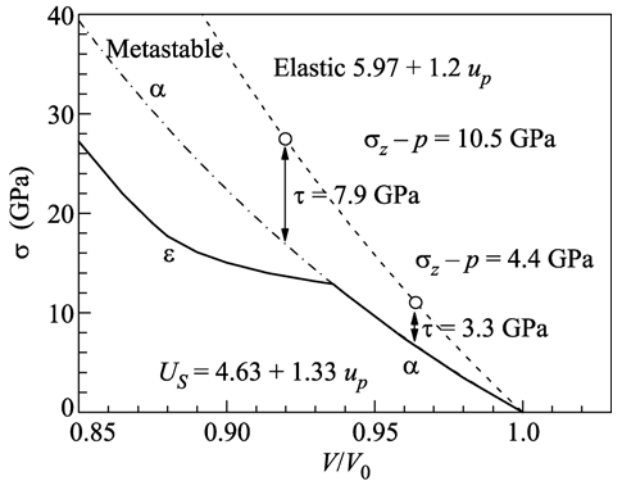

Fig. 5. Parameters of the state of iron behind the shock precursor front at distances of 250 and 540 nm.

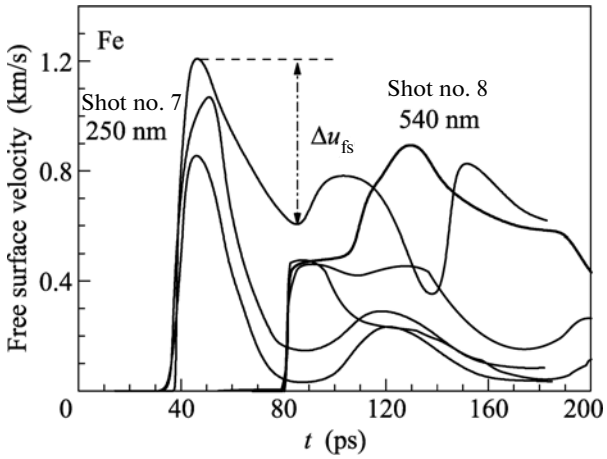

Fig. 6. Evolution of the compression wave in iron in the range from 250 to 540 nm at the energy density varying from 2.5 J/cm^2 in the center to 0.8 J/cm^2 in the peripheral part of the focal spot.

phase, the maximum shear stress τ was determined from the relation [21, 22]

$$\sigma_z(V) - p(V) = \frac{4}{3}\tau, \qquad (1)$$

where σ_z is the longitudinal elastic-compression stress. The values of 7.9 and 3.3 GPa were obtained.

Figure 6 shows two families of wave profiles of the free-surface velocity for the 250- and 540-nm-thick samples. Each of the families was obtained in one experiment. The profiles were plotted for various distances from the center of the focal spot of the laser pulse and correspond to various energy densities. A smooth increase in the velocity in the upper segment of the compression wave after the jump in shot no. 7 is not necessarily due to the beginning of plastic deformation and can be attributed to the intermediate stage of the formation of the shock wave at a given energy of the laser pulse.

The reflection of the compression pulse from the free surface of the sample results in the appearance of tensile stresses in the sample; the magnitude of these stresses increases as the reflected wave propagates from the surface to the bulk of the sample. When the tensile stresses exceed the strength of the material σ_{spall}, a fracture (spall) appears in the material [22, 23]. The relaxation of stresses at fracture leads to the formation of a secondary compression wave, the so-called spall pulse. Reaching the free surface, this pulse again increases the velocity of the surface. The tensile stress immediately before fracture is determined from the difference in the velocity Δu_{fs} between its maximum value and the value ahead of the spall pulse (Fig. 6). In the acoustic approximation, when the contribution of the nonlinearity of the compressibility of the material is insignificant, the characteristic method gives the simple formula $\sigma_{spall} = \rho_0 c \Delta u_{fs}/2$, where c is the speed of sound, for the calculation of the spall strength. High tensile stresses were achieved in our experiments and nonlinearity cannot be neglected. For this reason, to process the measurement results, we extrapolated the Hugoniot in (σ_z, u_p) coordinates to the region of negative pressures. This leads to the relation

$$\sigma_{spall} = \frac{1}{2}\rho_0(c_0 - b\Delta u_{fs}/2)\Delta u_{fs}, \qquad (2)$$

where c_0 and b are the coefficients in the linear expression for the Hugoniot $U_S = c_0 + bu_p$. An additional difficulty is due to possible elastic–plastic effects. With allowance for these effects, the formula for the calculation in the linear approximation for triangular load pulses has the more complex form

$$\sigma_{spall} = \rho_0 c_l \Delta u_{fs} \frac{1}{1 + c_l/c_b}, \qquad (3)$$

where c_b is the bulk speed of sound.

The spall strength was estimated from the experimental results for 250-nm-thick samples. For two peripheral profiles in Fig. 6, the maximum compression stress certainly does not exceed the elastic limit. Consequently, the spall fracture resistance can be estimated by Eq. (2) with the coefficients of the metastable elastic compression adiabat. The velocity decrements Δu_{fs} in these experiments were 0.96 and 0.83 km/s. The corresponding spall strengths are 20.3 and 17.8 GPa at a deformation rate of $\dot{V}/V_0 \approx (3–4) \times 10^8\ s^{-1}$. Plastic deformation apparently occurred in the center of the focal spot. Correspondingly, the spall strength was estimated by Eq. (3) with correction to the elastic–plastic behavior of the material. The estimated spall thickness (110 nm) indicates that the probability of spall at the boundary with a melted iron layer is high in this case. Figure 7 shows the resulting

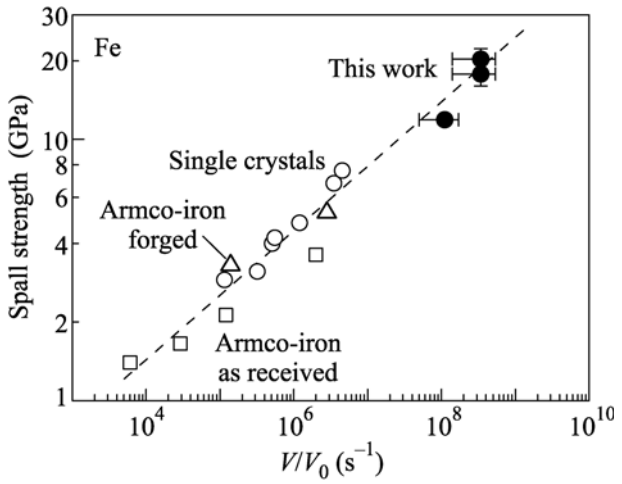

Fig. 7. Spall strength of iron measured for picosecond loads in comparison with the data obtained in the experiments with colliding plates [24].

spall strengths in comparison with the measurement results [24] for a longer shock load.

The ultimate shear strengths obtained in the ab initio calculations for iron are 7.2–7.5 GPa [25, 26]. The estimates from the measurement results reported in this work give the maximum value $\tau = 7.9$ GPa, which is even somewhat higher than the calculated ideal shear strength. However, it should be taken into account that compression is accompanied by an increase in the shear modulus and, correspondingly, in the ideal shear strength, which is proportional to the shear modulus. The ab initio calculations reported in [26, 27] give a value of 27.7–28.45 GPa for the ideal uniform tensile strength of iron. This value is slightly higher than the maximum spall strength of 20.3 GPa found from the measurement results. The ideal tensile strength under the uniaxial-tension conditions should be somewhat lower than that under uniform tension [27]. Furthermore, the ab initio calculations of the ideal shear and bulk strengths were performed for zero absolute temperature. At the same time, it is known that an increase in the temperature reduces these values. Thus, stressed states of iron, where these values are very close to the ideal strength values, have been achieved and measured with picosecond loads.

Unfortunately, owing to a strong nonstationarity of waves and a high rate of relaxation processes, the evolution of the state of the material after the achievement of the dynamic elastic stress could not be estimated. For this reason, the possibility of polymorphic transformations in the picosecond range of compression durations is an open problem and requires further investigations.

This work was supported by the State Atomic Energy Corporation ROSATOM (state contract no. N.4x.44.90.13.1111 on May 16, 2013) and by the Russian Academy of Sciences.

REFERENCES

1. S. I. Ashitkov, M. B. Agranat, G. I. Kanel, et al., JETP Lett. **92**, 516 (2010).
2. V. H. Whitley, S. D. McGrane, D. E. Eakins, et al., Appl. Phys. **109**, 013505 (2011).
3. J. C. Crowhurst, M. R. Armstrong, K. B. Knight, et al., Phys. Rev. Lett. **107**, 144302 (2011).
4. K. Kadau, T. C. Germann, P. S. Lomdahl, et al., Phys. Rev. B **72**, 064120 (2005).
5. B. J. Demaske, V. V. Zhakhovsky, N. A. Inogamov, et al., Phys. Rev. B **87**, 054109 (2013).
6. R. F. Smith, J. H. Eggert, R. E. Ruckl, et al., J. Appl. Phys. **110**, 123515 (2011).
7. S. I. Ashitkov, M. B. Agranat, G. I. Kanel, and V. E. Fortov, AIP Conf. Proc. **1426**, 1081 (2012).
8. V. P. Skripov, *Metastable Liquids* (Nauka, Moscow, 1972; Wiley, New York, Toronto, 1974).
9. M. Jahnátek, J. Hafner, and M. Krajčí, Phys. Rev. B **79**, 224103 (2009).
10. D. M. Chatterbuck, C. R. Krenn, M. L. Cohen, et al., Phys. Rev. Lett. **91**, 135501 (2003).
11. G. Kimminau, P. Erhart, E. M. Bringa, et al., Phys. Rev. B **81**, 092102 (2010).
12. G. I. Kanel, AIP Conf. Proc. **1426**, 939 (2012).
13. C. A. Bolme, S. D. McGrane, D. S. Moore, and D. J. Funk, J. Appl. Phys. **102**, 033513 (2007).
14. J. P. Geindre, P. Audebert, S. Rebibo, et al., Opt. Lett. **26**, 1612 (2001).
15. S. I. Ashitkov, P. S. Komarov, A. V. Ovchinnikov, et al., Quantum Electron. **43**, 242 (2013).
16. K. T. Gahagan, D. S. Moore, D. J. Funk, et al., J. Appl. Phys. **92**, 3679 (2002).
17. S. I. Anisimov, N. A. Inogamov, Y. V. Petrov, et al., Appl. Phys. A **92**, 797 (2008).
18. V. V. Temnov, K. Sokolovski-Tinten, P. Zhou, et al., J. Opt. Soc. Am. B **23**, 19554 (2006).
19. D. S. Moore, K. T. Gahagan, J. H. Reho, et al., Appl. Phys. Lett. **78**, 40 (2001).
20. L. M. Barker and R. E. Hollenbach, J. Appl. Phys. **45**, 4872 (1974).
21. Ya. B. Zeldovich and Yu. P. Raizer, *Physics of Shock Waves and High-Temperature Hydrodynamic Phenomena* (2nd ed., Nauka, Moscow, 1966; Academic, New York, 1966, 1967).
22. G. I. Kanel, S. V. Razorenov, and V. E. Fortov, *Shock-Wave Phenomena and the Properties of Condensed Matter* (Springer, New York, 2004).
23. G. I. Kanel, FFIMS **22**, 1011 (1999).
24. G. I. Kanel, S. V. Razorenov, and V. E. Fortov, Mech. Solids **40** (4), 69 (2005).
25. D. M. Clatterbuck, D. C. Chrzan, and J. W. Morris, Acta Mater. **51**, 2271 (2003).
26. S. Ogata, J. Li, N. Hirosaki, et al., Phys. Rev. B **70**, 104104 (2004).
27. M. Cerny and J. Pokluda, Phys. Rev. B **76**, 024115 (2007).

Translated by R. Tyapaev